

The Side-by-Side Urban Air Taxi Concept

Patricia Ventura Diaz*, Wayne Johnson†, Jasim Ahmad‡ and Seokkwan Yoon‡

NASA Ames Research Center, Moffett Field, California

High-fidelity computational fluid dynamics simulations have been carried out in order to analyze the aerodynamics and performance of the side-by-side urban air taxi for urban air mobility. High-order accurate schemes, dual-time stepping, and the delayed detached-eddy simulation model have been employed. The flow solver has been loosely coupled with a rotorcraft comprehensive analysis code. The vehicle simulated is a six-passenger side-by-side intermeshing rotor helicopter with hybrid propulsion for air taxi operations. This multi-rotor concept vehicle is intended to focus and guide NASA research activities in support of aircraft development for emerging aviation markets, in particular vertical take-off and landing air taxi operations.

I. Nomenclature

a	Fluid speed of sound
A	Rotor disk area, πR^2
c	Local rotor blade chord length
C'	Sectional chord force
c_{tip}	Rotor blade tip chord length
C_Q	Torque coefficient, $\frac{Q}{\rho(\Omega R)^2 R A}$
C_T	Thrust coefficient, $\frac{T}{\rho(\Omega R)^2 A}$
M'	Sectional blade pitching moment
M	Mach number, $\frac{V}{a}$
M_{tip}	Mach number at the blade tip, $\frac{\Omega R}{a}$
$M^2 c_c$	Sectional chord force coefficient, $\frac{C'}{\frac{1}{2} \rho a^2 c}$
$M^2 c_m$	Sectional pitching moment coefficient, $\frac{M'}{\frac{1}{2} \rho a^2 c^2}$
$M^2 c_n$	Sectional normal force coefficient, $\frac{N'}{\frac{1}{2} \rho a^2 c}$
N'	Sectional blade normal force
r	Radial position
R	Rotor radius
Re	Reynolds number, $\frac{V_{Ref}}{\nu}$
Re_{tip}	Reynolds number at the blade tip, $\frac{\Omega R c_{tip}}{\nu}$
V_∞	Freestream velocity
y^+	Non-dimensional viscous wall spacing
α	Angle of attack, AoA
δ	Boundary layer thickness
Δ	Grid spacing
μ	Advance ratio, $\frac{V_\infty \cos(\alpha)}{\Omega R}$
ν	Fluid kinematic viscosity
ρ	Fluid density
Ω	Rotor rotational speed

*STC

†Aeromechanics Office

‡NASA Advanced Supercomputing Division

II. Introduction

Electric multi-rotor vehicles have grown very popular over the past decade. While originally conceived for military purposes, their simplicity and affordability have made small drones, or Unmanned Aerial Vehicles (UAVs), accessible to the civil market. They are being used for photography, film recording, and also for recreational purposes, to name just a few applications. In addition, the unique ability of multi-rotor vehicles for vertical lift has great potential for human and cargo transportation in urban areas.



Figure 1: An artist impression of an urban air mobility environment, where air vehicles with a variety of missions and with or without pilots, are able to interact safely and efficiently.

NASA and a community of government, industry, and academic partners are working together on this goal, known as Urban Air Mobility (UAM). UAM is a safe and efficient air transportation system where everything from small package delivery drones to passenger-carrying air taxis operate over populated areas, from small towns to the largest cities. Figure 1 shows an artist's impression of an UAM environment, where different air vehicles move and interact safely in the airspace.

Relying on either fully electric or hybrid propulsion systems, the eVTOL (electrical Vertical Take-Off and Landing) vehicles would transport a small number of passengers from point to point in highly congested cities, avoiding ground traffic and potentially providing a greener means of transportation. Their capacity to hover and to perform VTOL, together with their great maneuverability, make multi-rotor vehicles an excellent choice for UAM aircraft.

Accurate prediction of rotorcraft performance and acoustics continues to be challenging from a computational point of view. The flows are inherently unsteady, nonlinear, and complex. The aerodynamic interactions between multiple rotors, fuselage, and lifting bodies make it even more difficult. High-fidelity Computational Fluid Dynamics (CFD) approaches offer an advantage over low- and mid-fidelity tools for this type of flow. In addition, high-fidelity simulations can provide the information needed to calibrate lower fidelity tools that could be used for design purposes.

The designs of conventional helicopters and airplanes have been well established and optimized during the twentieth century. However, the design space of eVTOL aircraft remains wide open, and exploration for improved designs continues. Previous computational work on small multi-rotor vehicles by Ventura Diaz et al.^{1,2} and Yoon et al.^{3,4} includes studies of the aerodynamic interactions, rotor placement, torque balanced coaxial octo-rotors, and the effect of wind gusts on a hovering quad-rotor. Johnson et al.⁵ and Silva et al.⁶ have recently conducted a comprehensive study for air taxi operations using multidisciplinary design, analysis, and optimization techniques, coming up with several multi-rotor UAM vehicle concepts.

This work focuses on analysis and simulations of one of these vehicle concepts: the Side-by-Side (SbS) UAM vehicle. The SbS vehicle has two overlapping intermeshing rotors, as represented in Figure 2. It is a six-passenger air taxi vehicle, with a range of 200 nm, thus performing four 50 nm trips without refueling. A typical UAM mission consists of multiple 50 nm segments.⁵ The SbS parallel hybrid propulsion system has two turboshaft engines, plus a motor/generator and a battery. The motor is used for hover and low



Figure 2: Hybrid side-by-side UAM concept. The two overlapping intermeshing rotors provide the required vertical lift in a more compact configuration.

speed flight, and in cruise the motor is driven as a generator by the turboshaft engine to charge the battery. The rotors of the side-by-side aircraft are overlapped by 15% (wingspan is 85% of the rotor diameter) for optimum cruise performance.⁶ In addition, the aircraft with overlapping rotors offers a more compact design, which is a preferred configuration in crowded urban environments.

The objective of the present work is to simulate and analyze NASA's side-by-side UAM concept using high-fidelity CFD. First, the results with the rotorcraft comprehensive analysis code CAMRAD II will be presented. Then, the high-fidelity Overflow CFD results for the intermeshing rotors, trimmed with the comprehensive code using a loose coupling approach, will be studied. The effects of different rotor overlap distances on airloads, rotor wake geometry and performance will be analyzed. The CFD results will be compared to the comprehensive code results. Finally, the complete vehicle will be studied and compared to the results of two side-by-side rotors without airframe.

Although there are no validation data for these simulations, the computations might assist in future validation testing.

III. Theory

The performance of a rotor system can be examined by means of the one-dimensional momentum theory.⁷ This theory uses the fluid mass, momentum, and energy conservation equations in an integral form. By using momentum theory, the ideal power P_i required to hover can be expressed as a function of the thrust T and the disk area A :

$$P_i = T v_i = T \sqrt{\frac{T}{2\rho A}} \quad (1)$$

where v_i is the induced velocity at the rotor disk. The disk loading is defined as $DL = T/A$. The power loading is the ratio of thrust to power, $PL = T/P$. Therefore, the induced (ideal) power loading is simply $(PL_i)^{-1} = P_i/T = v_i$.

In helicopter analysis, the rotor thrust coefficient C_T , the rotor power coefficient C_P and the rotor torque coefficient C_Q are formally defined as:

$$C_T = \frac{T}{\rho A \Omega^2 R^2} \quad (2)$$

$$C_P = \frac{P}{\rho A \Omega^3 R^3} \quad (3)$$

$$C_Q = \frac{Q}{\rho A \Omega^2 R^3} \quad (4)$$

where ρ is the flow density, A is the rotor disk area (for one rotor), Ω is the rotational speed and R is the radius of the blade. With $P = \Omega Q$, C_P and C_Q are identical.

The figure of merit (FM) is equivalent to a static thrust efficiency and is defined as the ratio of the ideal power required to hover to the *actual* power required, and it can be expressed as a function of the thrust and torque coefficients using momentum theory:

$$FM = \frac{\text{Ideal power required to hover}}{\text{Actual power required to hover}} = \frac{C_{P_i}}{C_P} = \frac{C_T^{3/2}}{\sqrt{2}C_Q} \quad (5)$$

Accurate prediction of the FM using high-fidelity CFD and hybrid turbulence models has been validated in previous studies.⁸

The operation of two or more rotors in close proximity will modify the flow field at each, and hence the performance of the rotor system will not be the same as for the isolated rotors. The limit case is the coaxial rotor, with just one-half the disk-area of the isolated rotors and therefore twice the disk loading. It follows that by operating the rotors coaxially the induced power required is increased by a factor of $\sqrt{2}$, a 41% hover induced power increase.

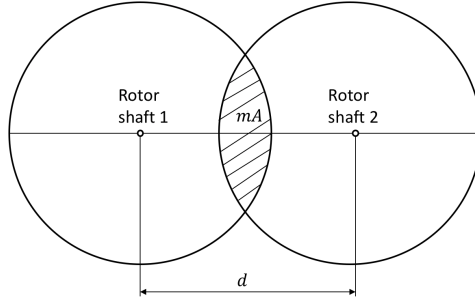


Figure 3: Twin rotor geometry involves the area of overlapping circles and the basic geometry of segments.

For hovering side-by-side twin rotors with overlap area mA , the hover performance estimate can be based on the effective disk loading of the system as a whole: $P = T\sqrt{T/2\rho A_{sys}}$, where the total area is $A_{sys} = A(2 - m)$. The ratio of the total power to that of the isolated rotors then is:

$$\frac{P}{P_{iso}} = \left(\frac{T}{T_{iso}}\right)^{3/2} \left(\frac{2}{2 - m}\right)^{1/2} \quad (6)$$

and for the same thrust the interference power is:

$$\frac{\Delta P}{P} = \left(\frac{2}{2 - m}\right)^{1/2} - 1 \quad (7)$$

In the coaxial limit this gives $\Delta P/P = 0.41$ as required.

Note that, with a shaft separation d , as seen in Figure 3, the overlap fraction is:

$$m = \frac{2}{\pi} \left[\cos^{-1} \frac{d}{2R} - \frac{d}{2R} \sqrt{1 - \left(\frac{d}{2R}\right)^2} \right] \quad (8)$$

IV. Numerical Approach

The flow solver used in this study is NASA's Overflow⁹ CFD solver. Overflow is a finite-difference, structured overset grid, high-order accurate Navier-Stokes flow solver. NASA's Chimera Grid Tools (CGT)¹⁰ overset grid generation software is used for generating the overset grids of rotors and complete vehicles. Body-fitted curvilinear near-body (NB) grids are generated using CGT. The computational domain is completed with the generation of Cartesian off-body (OB) grids that are automatically generated prior to grid assembly using the domain connectivity framework in Overflow-D mode. The current time-accurate approach consists of an inertial coordinate system where NB curvilinear O-grids for the rotor blades rotate

through the fixed OB Cartesian grid system. Overflow is coupled in a loosely manner with the helicopter comprehensive code CAMRAD II.¹¹ The CFD provides high-fidelity, nonlinear aerodynamics that replace the comprehensive lifting line aerodynamic analysis from CAMRAD II. The comprehensive code performs the structural dynamics and trim calculations and gives the information to Overflow. The loose coupling allows for a modular approach and communication through input/output. The coupling methodology has been implemented following the approach of Potsdam et al.¹²

The numerical approach and the coupling process are described below.

A. Overset Grid Generation

The overset grid generation process using CGT can be divided into the following steps: geometry processing, surface grid generation, volume grid generation, and domain connectivity.¹⁰

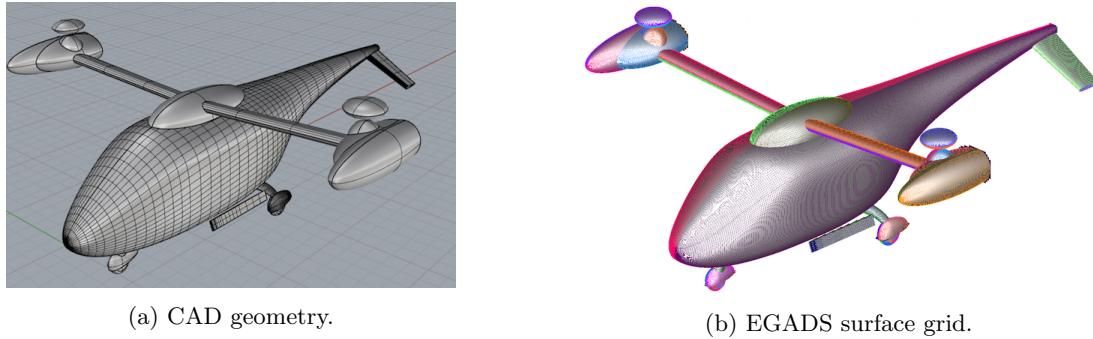


Figure 4: The side-by-side fuselage. The image on the left shows the CAD geometry, the image on the right shows the structured untrimmed patches obtained from the CAD geometry using EGADS. The patches are used as reference surfaces to generate the overset surface grids.

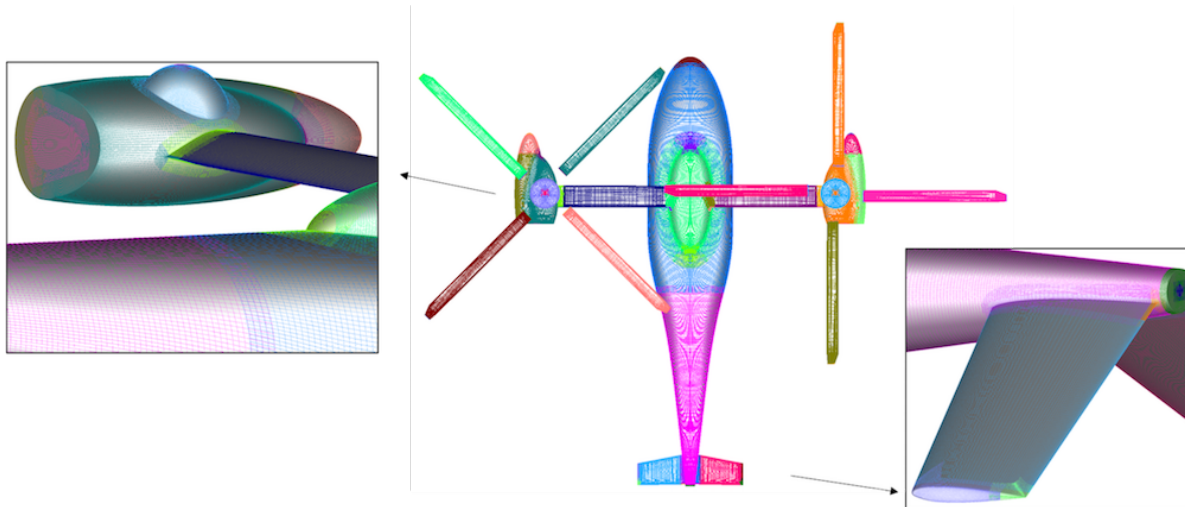


Figure 5: Side-by-side overset surface grids, top view. On the left, the attachment of the engine with the wing is shown in detail. The image on the right shows the attachment of the tail to the fuselage.

The geometry is usually obtained from a Computer Aided Design (CAD) model. Figure 4a shows the CAD model of the SbS vehicle. The Boundary Representation (BRep) is an object that holds both the topological entities and the geometric components.¹³ In this work, a pre-processing step converts the analytical BRep solid from a STEP or IGES file into discrete representations for the BRep faces and edges. Access to the model topology and entities is accomplished through EGADS (the Engineering Geometry Aerospace Design System) API which is a foundational component of the Engineering Sketch Pad.¹³ With the *egads2srf* tool, discrete representations are generated from each solid. Figure 4b shows the structured surface grid file for the

SbS obtained using EGADS. This grid file contains an untrimmed structured patch for each face based on tessellation of the face parameter space. Another file obtained with *egads2srf* is a curve grid file containing tessellated edges. The curve grid file and the structured grid file from EGADS are used as an input for the overset surface grid generation step.

Overset structured surface meshes are typically created using a combination of algebraic and hyperbolic methods, depending on the number of initial curves on each surface domain. The generation of surface grids is the step that requires the most manual effort and expertise from the user. Figure 5 shows the surface grids for the SbS vehicle with the rotors. For this study, the landing gear and the strakes have been omitted. The grid system consists of the main fuselage, the wing, the engines, the tail, the rotors, and the rotor hubs.

With sufficient overlap between surface grids, the volume grids can be created easily with hyperbolic marching methods out to a fixed distance from the surface. Such methods provide orthogonal grids with tight clustering characteristics at the wall, which is essential for accurately capturing the boundary layer in viscous flow computations. The distance is chosen such that the outer boundaries of the NB volume grids are well clear off the boundary layer. The NB grids are then embedded inside OB Cartesian grids that extend to the far field. Figure 6a shows the near-body grids for the SbS with rotors, in Figure 6b the NB and the OB Cartesian grids are shown.

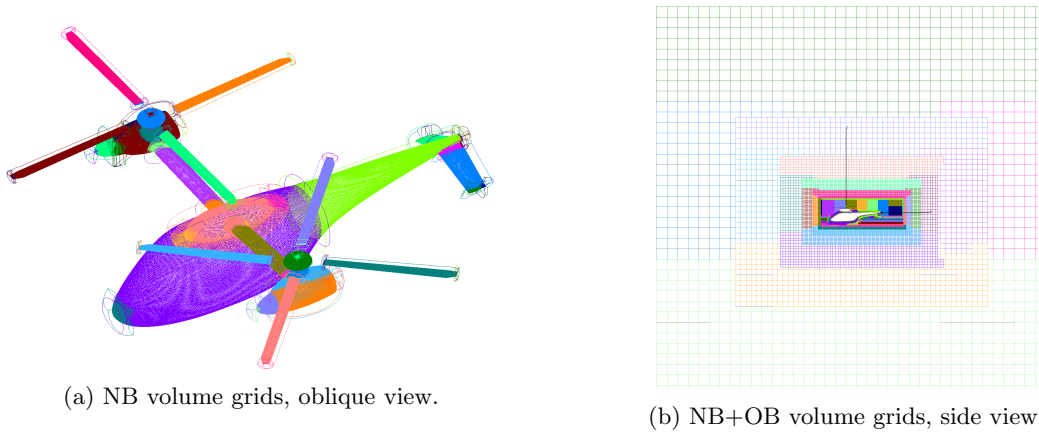


Figure 6: Side-by-side overset volume grids. Figure a shows the boundary edges of the near-body volume grids. Figure b shows the near- and off-body Cartesian volume grids.

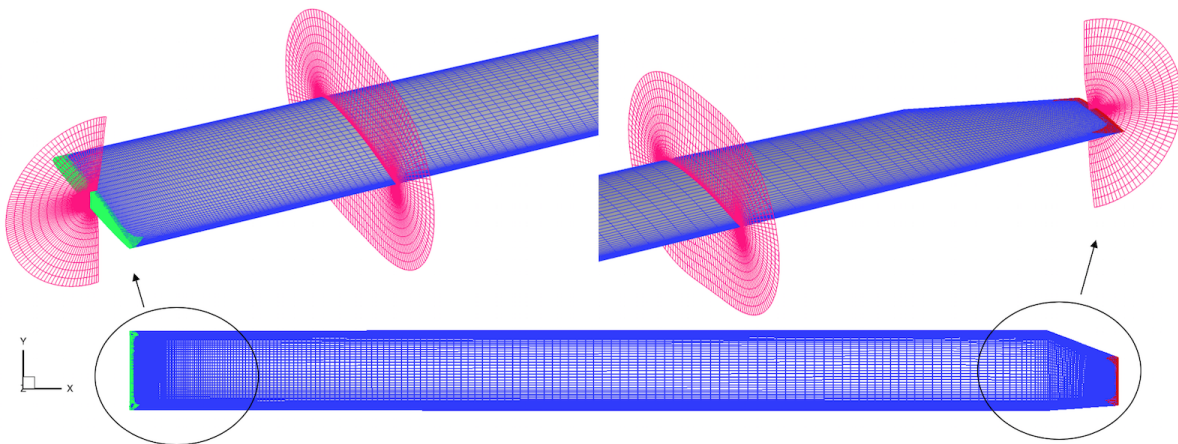


Figure 7: Blade overset grids for the side-by-side urban air taxi. The NB root and tip grids are shown in detail. Cap grids are used for the root (green) and tip (maroon), O-grids are used for the blade (blue). Slices of the volume grids are shown in magenta. There is clustering near the leading edge, trailing edge, blade tip and blade root, in order to solve the large pressure gradients near these regions.

Off-body Cartesian grids with uniform spacing surround the NB grids to resolve the wake region of interest. Coarser Cartesian grids efficiently expand the grid system to the far field, where each successive Cartesian grid is twice as coarse as its previous neighbor. The far field boundary is 20 rotor radii away from the center of the vehicle in all directions. The resolved wake region has a uniform grid spacing of 10% of the tip chord length c_{tip} .

The airframe grids have been generated using the CAD model shown in Figure 4a as reference. For the blade grid generation, the rotor geometry information from Table 1 has been used. The profiles used to build the blade are the VR12 airfoils from $r = 0$ to $r = 0.85R$, and the SSCA09 airfoils from $r = 0.95R$ to the tip, $r = R$. The transition between the two different airfoil sections is smooth (linear interpolation with the radial stations). The blade is tapered and swept near the tip. Figure 7 shows in detail the SbS blade. Surface grid resolution on the rotor blades is clustered in the chordwise direction near the airfoils leading and trailing edges to accurately resolve large pressure gradients. Subsequently, the spanwise resolution is clustered near the root and the tip. The normal grid spacing of all grids at the walls maintains $y^+ \leq 1$.

Number of rotors	2
Number of blades/rotor	4
Radius, R	3.203 m
Linear twist	-16 deg
Root chord, c_{root}	0.217 m
Tip chord, c_{tip}	0.130 m
Rotor solidity, σ	0.0832
Nominal tip speed, V_{tip}	167.6 m/s

Table 1: Side-by-side rotor geometry properties.

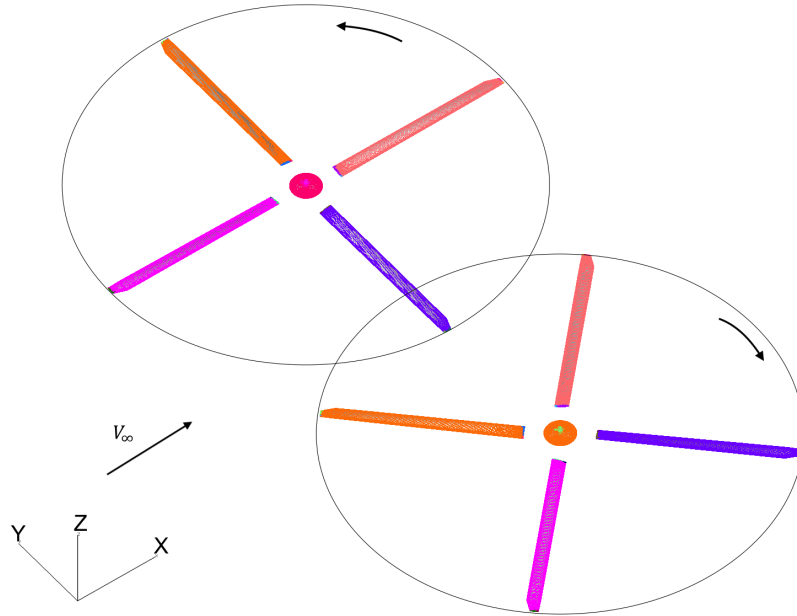


Figure 8: Side-by-side rotors overset grids with 15% overlap. The overlapping distance is changed in order to study its effect on airloads, performance and rotor wake geometry.

The multi-rotor system consists of two overlapping rotors, each rotor made up of four blades. The right rotor rotates counter-clockwise (CCW), and the left rotor rotates clockwise (CW), therefore the advancing blade is always outboard. The rotor grids without airframe with 15% overlap are shown in Figure 8. The overlapping distance can be changed and its effect on the airloads, performance, and wake geometry in cruise

will be the main subject of study in the present work. For example, Figure 9 shows the front view grid system of the side-by-side isolated rotors.

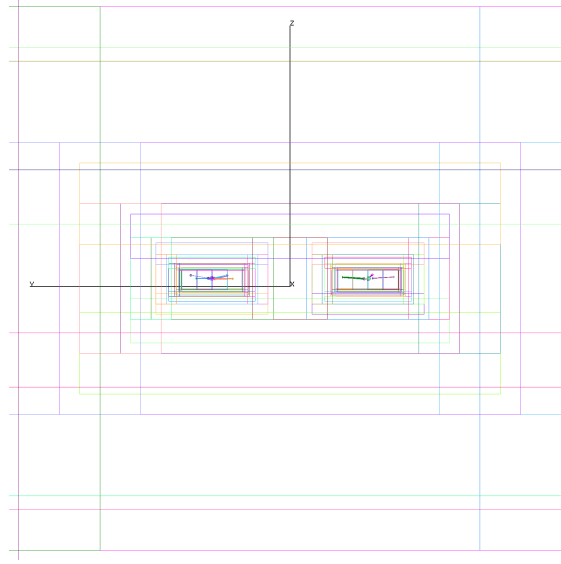


Figure 9: Front view of the side-by-side isolated rotors grid system. The distance between the rotor rotational centers is $3D$, where D is the rotor diameter.

The rotor system consists of 30 NB grids with 25 NB million grid points, and 235 to 260 million total (NB + OB) grid points, depending on the overlapping distance. For the complete vehicle, there is a total of 74 NB grids with 40 NB million grid points, the total number of NB and OB grid points is 300 million.

By using a trimmed approach, the domain connectivity step is robust and highly automated. In this study, the X-ray hole cutting method is used. An X-ray object is created for every component in the geometry (i.e. the blades, the hubs, the fuselage, the wings, etc.). The user has to supply the list of meshes that each X-ray object is allowed to cut, and an offset distance with which to grow each hole away from the body. Hole cutting is required between components and with the OB Cartesian grids. The hole cutting process is performed at each time step within the flow solver, allowing for the rotation of the blades relative to the fixed components.

B. High-Order Accurate Navier-Stokes Solver

Overflow solves the Navier-Stokes equations using finite differences with a variety of numerical algorithms and turbulence models. The time dependent, Reynolds-averaged Navier-Stokes (RANS) equations are solved in strong conservation form.

$$\frac{\partial \vec{q}}{\partial t} + \frac{\partial(\vec{F} - \vec{F}_v)}{\partial x} + \frac{\partial(\vec{G} - \vec{G}_v)}{\partial y} + \frac{\partial(\vec{H} - \vec{H}_v)}{\partial z} = 0 \quad (9)$$

where $\vec{q} = [\rho, \rho u, \rho v, \rho w, e]^T$ is the vector of conserved variables; \vec{F} , \vec{G} and \vec{H} are the inviscid flux vectors; and \vec{F}_v , \vec{G}_v and \vec{H}_v are the viscous flux vectors.

In this study, the diagonal central difference algorithm is used with the 5th-order accurate spatial differencing option with scalar dissipation. The physical time step corresponds to 0.25 degree rotor rotation, together with up to 50 dual-time sub-iterations, to improve time-accuracy by reducing the linearization errors. The numerical approach and time step were previously validated for various rotor flows.^{8,14,15}

C. Hybrid Turbulence Modeling

The Overflow code has a choice of algebraic, one-equation, and two-equation turbulence models, including hybrid Reynolds-Averaged Navier-Stokes / Large Eddy Simulation (RANS/LES) models that close the RANS

equations. In this study, the one equation Spalart-Allmaras¹⁶ turbulence model is used primarily within the boundary layer.

The intent of the Detached Eddy Simulation (DES) model¹⁶ is to be in RANS mode throughout the boundary layer, where the turbulent scales can be very small and need to be modeled, and in LES mode outside the boundary layer where the largest turbulent scales are grid-resolved. In this way, DES is a RANS/LES hybrid approach that mitigates the problem of artificially large eddy viscosity. The turbulence length scale d is replaced by \bar{d} , where \bar{d} is the minimum of the distance from the wall, d , and the local grid spacing times a coefficient.

The DES approach assumes that the wall-parallel grid spacing Δ_{\parallel} exceeds the thickness of the boundary layer δ so that the RANS model remains active near solid surfaces. If the wall-parallel grid spacing is smaller than the boundary layer thickness, $\Delta_{\parallel} < \delta$, then the DES Reynolds stresses can become under-resolved within the boundary layer; this may lead to non-physical results, including grid-induced separation. Using Delayed Detached Eddy Simulation (DDES),¹⁷ the RANS mode is prolonged and is fully active within the boundary layer. The wall-parallel grid spacing used in this study does not violate the hybrid-LES validity condition; thus DES and DDES should give similar results. Nevertheless, all computations have been performed using the DDES model for both NB and OB grids.

D. Comprehensive Analysis

Structural dynamics and rotor trim for the coupled calculations are performed using the comprehensive rotorcraft analysis code CAMRAD II.¹¹ CAMRAD II is an aeromechanics analysis of rotorcraft that incorporates a combination of advanced technologies, including multibody dynamics, nonlinear finite elements, and rotorcraft aerodynamics. The trim task finds the equilibrium solution for a steady state operating condition, and produces the solution for performance, loads, and vibration. The aerodynamic model for the rotor blade is based on lifting-line theory, using two-dimensional airfoil characteristics and a vortex wake model. CAMRAD II has undergone extensive correlation with performance and loads measurements on rotorcraft.

E. Loose Coupling Overflow – CAMRAD II

A loose coupling approach between Overflow and CAMRAD II based on a trimmed periodic rotor solution is implemented. The comprehensive code provides the trim solution and blade motions. The high-fidelity CFD calculates the airloads. Figure 10 shows the flow diagram of the loose coupling strategy. In summary, the CFD airloads replace the comprehensive airloads while using lifting line aerodynamics to trim and computational structural dynamics to account for blade deformations. In this work, the SbS blades have flap hinges, but are considered rigid, and consequently there will not be elastic motions in the blades. The comprehensive analysis is still needed to get the trim angles and rigid blade motions for the CFD.

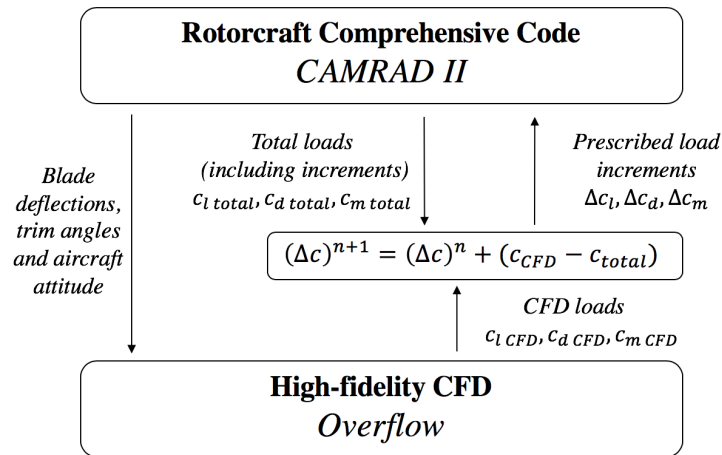


Figure 10: Flow diagram for CFD/Comprehensive Analysis loose coupling methodology.

The iterative loose coupling process is summarized next. The simulation is initialized with a comprehensive analysis resulting in a trimmed rotor solution obtained with lifting line aerodynamics. This analysis creates initial quarter chord motions as a function of the radius r and the azimuth ψ , for each rotor. In addition, the aircraft attitude is also obtained from CAMRAD II. The motions and aircraft pitch angle are given to the CFD. The CFD analysis accounts for the entire flow field, and therefore it only requires the structural motion. The CFD is run with the prescribed motions and angles, for two to three full rotor revolutions for the first coupling step. Overflow outputs the normal force N' , pitching moment M' , and chord force C' as a function of radius and azimuth.

Then, the aerodynamic force and moment coefficients increments (Δc) that are used in the comprehensive code at the next iteration $n+1$ are calculated. The increments are the difference between the CFD loads and the comprehensive lifting line solution required to trim from the previous step n , plus the load increments from the previous step:

$$(\Delta c)^{n+1} = (\Delta c)^n + (c_{CFD} - c_{total}) \quad (10)$$

For the initial step, the increments are the difference between CFD and the total loads from the 0^{th} run in CAMRAD II:

$$(\Delta c)^1 = (c_{CFD} - c_{total})$$

The sectional pitching moment $M^2 c_m$, normal force $M^2 c_n$ and chord force $M^2 c_c$ coefficients are defined as:

$$M^2 c_m = \frac{M'}{\frac{1}{2} \rho a^2 c^2} \quad (11)$$

$$M^2 c_n = \frac{N'}{\frac{1}{2} \rho a^2 c} \quad (12)$$

$$M^2 c_c = \frac{C'}{\frac{1}{2} \rho a^2 c} \quad (13)$$

With the new quarter chord motions of the retrimmed rotor and the new aircraft attitude, the CFD is rerun. The previous CFD flow solution is used as restart condition. The coupling is performed every half or quarter rotor revolution. The coupling solution is considered to be converged when collective and cyclic control angles and the CFD aerodynamic forces do not change between iterations. The CFD flow solution is usually converged after 10 to 20 rotor revolutions.

The coupling procedure is valid as long as the rotor loads are periodic. This approach is still good if there is some aperiodicity in the vortex wake, which is often the case in high-resolution turbulent simulations.

The coupled Overflow – CAMRAD II simulations are completely automatized using a Python code and Fortran post-processing functions. All simulations were run on NASA’s supercomputers Pleiades and Electra, using from 2000 to 2500 cores on SandyBridge, Broadwell, and Skylake nodes.

V. Results

The comprehensive rotorcraft code CAMRAD II and the high-fidelity CFD code Overflow are used throughout this study to simulate the side-by-side urban air taxi in edgewise forward flight. The main flow features and parameters used in forward flight are presented in Figure 11, for a rotor rotating CCW. For a CW rotor, the direction of the azimuth ψ is reversed.

First, the side-by-side vehicle performance are obtained using CAMRAD II, with its free wake model. Then, the loosely coupled Overflow - CAMRAD II simulations for the intermeshing rotors without airframe are run, for different rotor overlaps. Finally, the complete vehicle simulated with CAMRAD II - Overflow will be presented.

CAMRAD II provides the trim solution and the rigid motion of the blades to Overflow. Overflow solves the Navier-Stokes flow equations with the rotor information. The loosely coupled methodology provides a more accurate strategy to calculate the rotor loads.

interaction inboard.

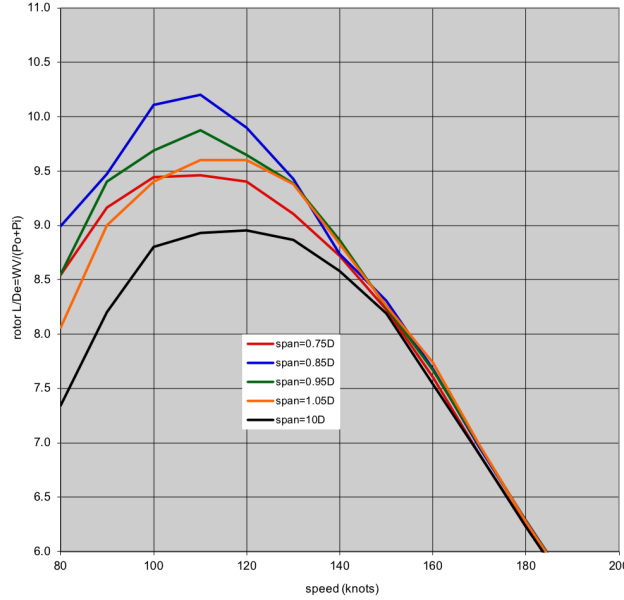


Figure 12: Twin rotor free wake performance calculations of rotor efficiency L/D_e . Results show that a $0.85D$ wing span (15% rotor overlap) is the most efficient configuration in cruise.

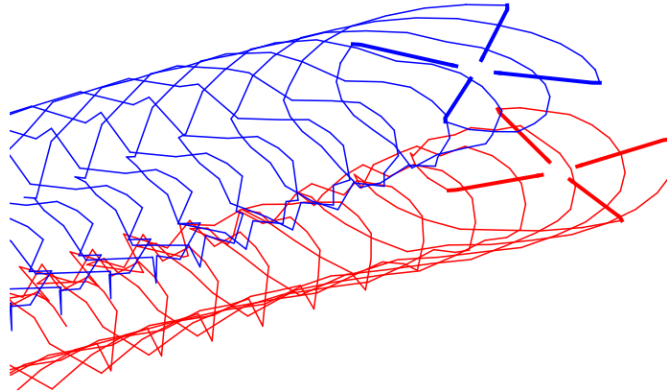


Figure 13: Wake geometry for the side-by-side rotors obtained with CAMRAD II, for 15% overlap. There is wake rollup with two large super-vortices outboard and a weak interaction inboard.

B. Overflow - CAMRAD II Results: SbS Rotors in Edgewise Flight

The side-by-side rotors without airframe are simulated in forward flight using the Overflow - CAMRAD II loosely coupled strategy described in the Numerical Approach section, using the overset grid system shown in Figure 8. Five different wing spans are considered in this work: $0.75D$ (25% overlap), $0.85D$ (15% overlap), $0.95D$ (5% overlap), $1D$ (0% overlap) and $3D$ spans (isolated rotors). The $3D$ span case is representative of *isolated* side-by-side rotors. Yoon et al.¹⁵ showed that the normalized vertical force coefficient of rotors with an inter-rotor separation of $2D$ (wing span = $3D$) is 99.9% that of the isolated single rotor in hover conditions. Therefore, the $3D$ span case represents the isolated rotor case. The grid system of the side-by-side isolated rotors is shown in Figure 9.

From the comprehensive analysis study described in the previous paragraphs, the rotors with 15% overlap have been found to be the most efficient in cruise, and thus the nominal case for study in the coupled simulations will be the side-by-side rotors with 15% overlap distance.

The flight condition simulated is the best-range cruise, at 5000 ft ISA +20°C, with an advance ratio of $\mu = 0.356$. Table 2 summarizes the flow conditions.

h	5000 ft
T_∞	ISA +20°C
V_∞	115 kts
N	499.7 rpm
M_{tip}	0.484
M_∞	0.172
μ	0.356
Re	$1.9 \cdot 10^6$

Table 2: Best range cruise flow conditions for the side-by-side urban air taxi CFD simulations.

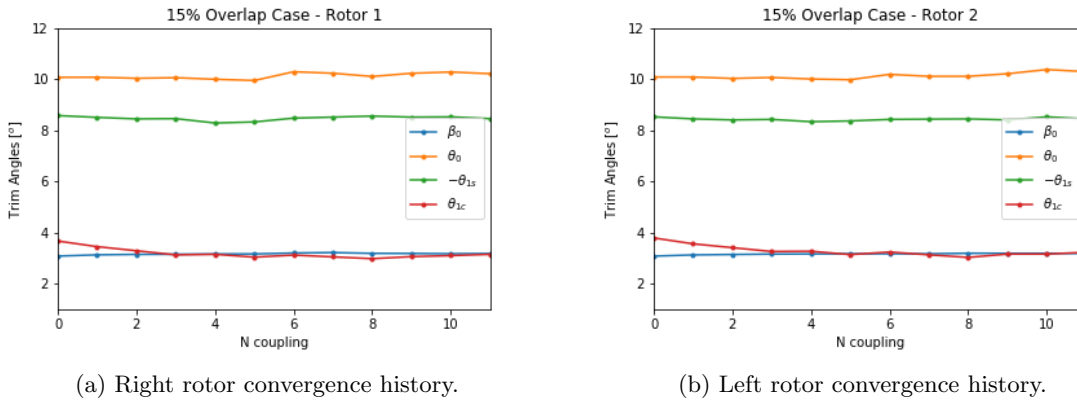


Figure 14: Loose coupling angles convergence history, for intermeshing rotors with 15% overlap. There is no 1/rev flapping or lag motion.

The Overflow - CAMRAD II coupling approach is considered to be converged when the trim angles do not change from one coupling step to the next, or when this change is relatively small. Figure 14 shows the trim angles history, for the right and left rotors (rotor 1 and rotor 2, respectively) in the 15% overlap case. Loose coupling convergence is reached after less than 10 coupling steps. As mentioned earlier, the cyclic pitch trims the 1/rev flapping to zero.

Airloads

The airloads for the side-by-side rotors with 15% overlap are shown in Figures 15 and 16. Figure 15 shows the mean normal force coefficient c_n , chord force coefficient c_c , and pitch moment coefficient c_m , as functions of the radial distance r/R , for the right and left rotors, and for the isolated side-by-side rotors (span = $3D$). The sectional coefficients are multiplied by the square of the sectional Mach number M . The mean is obtained by averaging over a complete rotor revolution, $0 \leq \psi < 360$, where ψ is the azimuth. There are some asymmetries between the right and left rotor airloads, and the differences slightly increase near the tip. They are probably due to the turbulent character of the vortex wake. The mean sectional airload values for the other overlap distances (25%, 5% and 0%) are very similar to the 15% case. In the case of the isolated side-by-side rotors, the airloads on the left and right rotors are identical, hence only one rotor is represented with the dashed black lines in Figures 15 and 16, and it is designated as “Isolated SbS rotor”. The distribution of mean normal force and chord coefficients is relatively lower for the isolated rotors case compared to the rotors with 15% overlap. In consequence, the integrated vertical and horizontal forces, that is, the lift L and propulsive X forces, of the rotor system, will be smaller for the isolated twin rotor system than for side-by-side rotors with some overlap.

The azimuth variations of the computed sectional loads at four radial stations are shown in Figure 16.

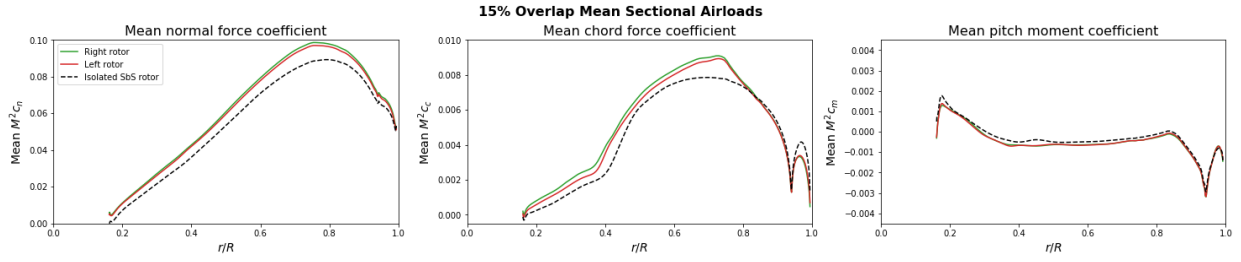
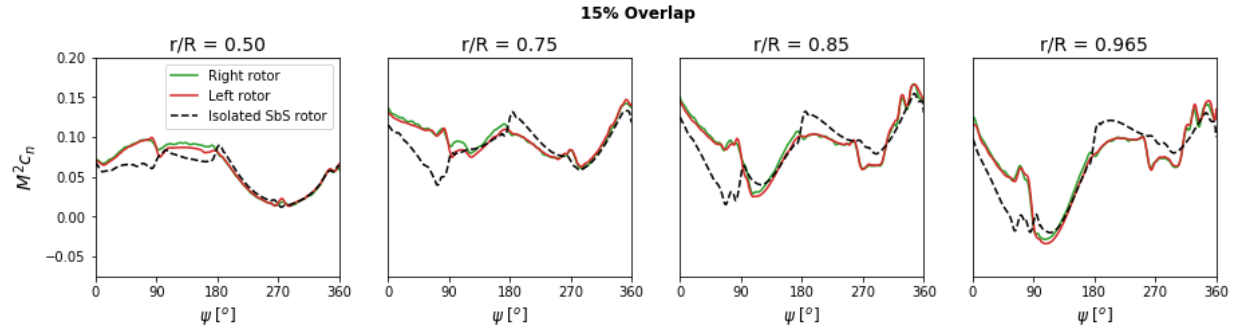
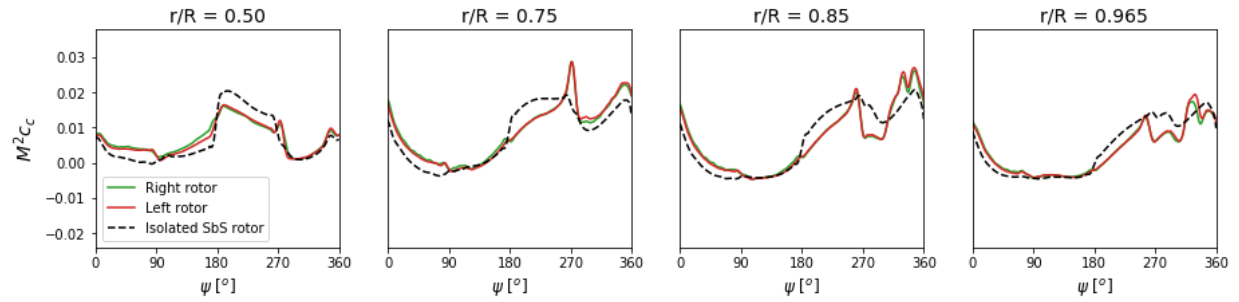


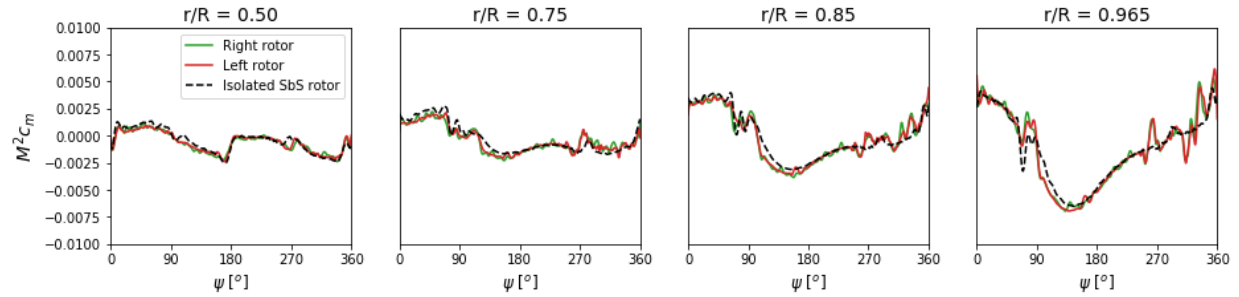
Figure 15: Mean sectional airloads for two side-by-side rotors with an overlap distance of 15%, $\mu = 0.356$. The right rotor is represented by the green lines, and the left rotor by the red lines. The dashed black lines represent the mean airloads of the side-by-side isolated rotor.



(a) Normal force coefficient, $c_n M^2$, at four different radial stations.



(b) Chord force coefficient, $c_c M^2$, at four different radial stations.



(c) Pitch moment coefficient, $c_m M^2$, at four different radial stations.

Figure 16: Azimuthal distribution of airloads for two side-by-side rotors with an overlap distance of 15% . The right rotor is represented by the green lines, and the left rotor by the red lines. The dashed black lines represent the airloads of the side-by-side isolated rotor.

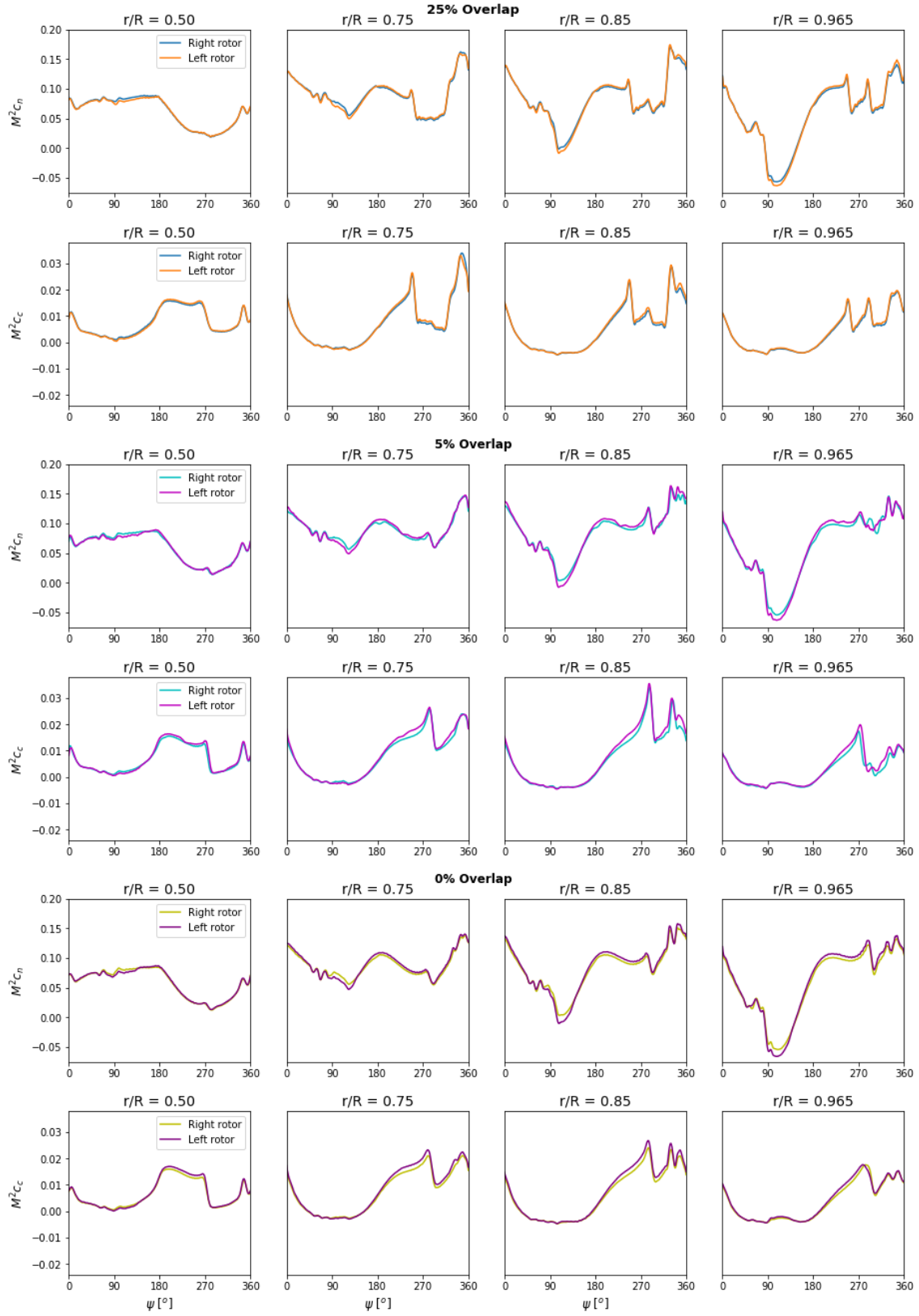


Figure 17: Airloads distribution for two side-by-side rotors for three overlap distances, 25%, 15% and 0%, at four radial stations. The first row of each overlap distance shows the normal force coefficient, and the second row shows the chord force coefficient.

The radial stations considered in this study are $r/R = 0.5$, $r/R = 0.75$, $r/R = 0.85$, and $r/R = 0.965$. Figure 16a shows the normal force coefficient $c_n M^2$. The normal force coefficient varies significantly with the azimuth at each radial station. For the most outboard location, $r/R = 0.965$, for the left and right rotors with 15% overlap, the peaks observed near $\psi = 90^\circ$ and $\psi = 270^\circ$ are the consequence of blade-vortex interaction (BVI). The peaks before $\psi = 360^\circ$ are due to the separated wake from the hubs, and they can be observed at the four radial stations. There is also BVI for the isolated SbS rotors, see the peaks near $\psi = 90^\circ$ and the small peak near $\psi = 270^\circ$.

The nomenclature from Figure 11 for a rotor in forward flight rotating CCW will be used in the following paragraphs. From the airloads distribution we can identify three BVI events happening on the rotor:

1. BVI near $\psi = 90^\circ$ (advancing side), seen by the peak in normal force near the tip of the blade. The BVI is from the vortex trailed by the previous blade of the same rotor.
2. BVI before $\psi = 270^\circ$ (retreating side). In this case, the vortex is coming from the blade of the opposite rotor. This is a strong BVI event.
3. BVI right after $\psi = 270^\circ$ (retreating side), see the smaller peak right after the peak from BVI from the opposite rotor. This time again, the vortex is trailed by the previous blade of the same rotor.

In single rotors, the BVI observed are the BVI events (1) and (3) described previously. BVI event (2) is characteristic of SbS overlapping rotors.

Figure 16b shows the chord force coefficient. The peaks in chord force appear near the beginning and end of the overlap region; that also agrees well with the BVI events. The pitch moment coefficient is shown in Figure 16c. The variations of the pitching moment along the azimuth are relatively smaller.

In all the cases, for all the radial stations, there are fluctuations near $\psi = 360^\circ$, where the blades are downwind and immersed in the separated wake of the hub.

The effect of the overlap distance on the airloads can be observed on Figure 17. The first two rows show the normal and chord coefficients ($M^2 c_n$, $M^2 c_c$) for four different radial stations for two side-by-side rotors with an overlap of 25%. The third and fourth row are for an overlap distance of 5%. The last two rows represent the case with 0% overlap.

For the 25% overlap distance (rows one and two of Figure 17), the three BVI events can be seen even more clearly than for the 15% overlap case. This time, with a 25% overlap, there is only 50% of the radius that is out of the overlap zone at $\psi = 270^\circ$. The BVI events happening on the retreating side appear to be equally strong near the tip; see the last column of rows one and two (25% overlap: $M^2 c_n$ - mean, $M^2 c_c$ - mean) of Figure 17, $r/R = 0.965$. The BVI events at the retreating side can also be observed further from the tip, at $r/R = 0.85$. With a rotor separation of $0.85D$, the double BVI event near $\psi = 270^\circ$ was clearly depicted in the outermost radial station ($r/R = 0.965$), but not in the $r/R = 0.85$ station. The second BVI event appears to be stronger at this radial station. Traveling further inboard, $r/R = 0.75$, the third BVI event is no longer observable on the force coefficients. There is a relatively stronger peak on the chord force for the second BVI event.

The third and fourth rows of Figure 17 represent the case with 5% overlap. The BVI events near $\psi = 270^\circ$ happen very close to each other due to the reduced overlap distance. In addition, there seem to be some discrepancies between the left and right rotor airloads near this region; this is probably caused by the turbulent character of the vortex wake. When looking at the chord force coefficient distribution, there is a single large peak at $r/R = 0.85$, instead of the two peaks observed with 25% overlap, which suggests a combination of both BVI events in one single stronger event for certain radial stations.

The last two rows of Figure 17 show the normal and chord force coefficient for two side-by-side rotors with 0% overlap. There is still interference between the two rotors because each rotor is operating in the upwash flow field of the other rotor. In this case, there is only BVI from vortices trailed by the blades from the same rotor.

When comparing the airloads for the different overlaps at the innermost radial station represented here, $r/R = 0.5$, the distributions seem very similar to each other; see the first column of Figures 16 and 17. That is, outside of the overlap zone, the airloads do not change for different overlaps. However, there is a significant difference on airload distribution with the side-by-side isolated rotors, for all radial stations, see Figures 16a, 16b and 16c.

Overall, there are important interactions between the rotors that affect the airload distributions. The BVI event from the vortices originating from the opposite rotor changes with the overlap distance. The right

and left rotors have similar airload distributions, and the small dissymmetries are probably caused by the turbulent character of the vortex wake.

Rotor Disk Forces

Figure 18 shows the rotor disk normal force coefficient $M^2 c_n$ for the side-by-side rotors for 25%, 15%, 5% and 0% overlap distances. The grey dashed lines represent the overlap region. For a reminder of the flow features and parameters in forward flight on the rotor disk, the reader should refer to Figure 11.

On the advancing side of the blade and near the tip the normal force is relatively smaller, see blue regions of Figure 18. The effect on the normal force from the interactions between the rotor blades can be seen around the azimuth $\psi = 270^\circ$; see the orange-yellow regions, between $225^\circ < \psi < 270^\circ$, followed by green regions (lower normal force) before $\psi = 270^\circ$, for the cases with 25% and 15% overlap. In the 5% case, the affected region is smaller but the magnitude of the normal force is relatively higher. For 0% overlap, there is a region after $\psi = 270^\circ$. Even if the rotors are not overlapped, there are still rotor-rotor interactions. The regions of higher normal force downstream near $\psi = 360^\circ$ are due to the separated wake of the hub.

When comparing the right rotor (CCW) and the left rotor (CW), there is symmetry between the force coefficients, and the slight differences are not unexpected. Overflow is solving the unsteady Navier-Stokes equations, and a small assymetry between rotors is normal.

The chord force coefficients on the rotor disk for 25%, 15%, 5% and 0% overlaps are shown in Figure 19. The main interest of these images is the clear effect of the overlap distance on the polar plots. These images agree well with the linear plots from Figures 16 and 17. The chord force coefficient is relatively strong near the overlapping regions and on the separated flow from the hub. The chord force coefficient value around the overlapping zone increases when the overlapping distance decreases.

The pitch moment coefficient distributions on the rotor disk for different overlap distances are shown in Figure 20. The pitch moment coefficient distribution does not seem to be affected by the overlapping distance. The distribution of c_m on the rotor disk is such that the integrated moment is zero, thanks to rotor trimming.

Finally, Figure 21 shows the normal force coefficient, chord force coefficient and pitch moment coefficient for the isolated rotors. The normal and chord force coefficient distribution is different from the distributions with rotor overlap. The distributions are mostly smooth, and there are no peaks near the $\psi = 270^\circ$. The pitch moment coefficient distribution is very similar to previous cases.

Wake Geometry

The vortex wakes for 25%, 15%, 5% and 0% overlap distances are shown in Figures 22, 23, 24, and 25, respectively. The vortex wake of the side-by-side isolated rotors is shown in Figure 26. The vortices are visualized by using iso-surfaces of the Q-criterion vorticity, and they are colored with the vorticity magnitude. All figures use the same values of Q-criterion and vorticity magnitude.

Some common flow features that appear in the vortex wakes of the four cases with overlap (25%, 15%, 5% and 0%^a) and for the side-by-side isolated rotors, are summarized here:

- Blade-vortex interactions.
- Blade tip-vortex rollup downstream at the exterior (advancing side) of both rotors.
- Interaction in the overlap region (retreating side) of one vortex wake with another.
- Development of worm-like vortical structures¹⁸ in the downstream wake.
- Separated wake flow from the hubs.

The rotor-rotor interactions are stronger when the rotors are closer. An interesting flow feature can be observed for the 0% case: the vortices from each rotor do not interact in the beginning; however, further downstream there are clear interactions and vortex wrapping and rolling can be seen.

^aEven with 0% overlap there are rotor-rotor interactions, as it has been observed throughout this study. In fact, the separation needed for removing rotor-rotor interactions, is of two rotor diameters ($2D$), thus the rotors rotational centers are separated by $3D$, as demonstrated by Yoon et al.¹⁵

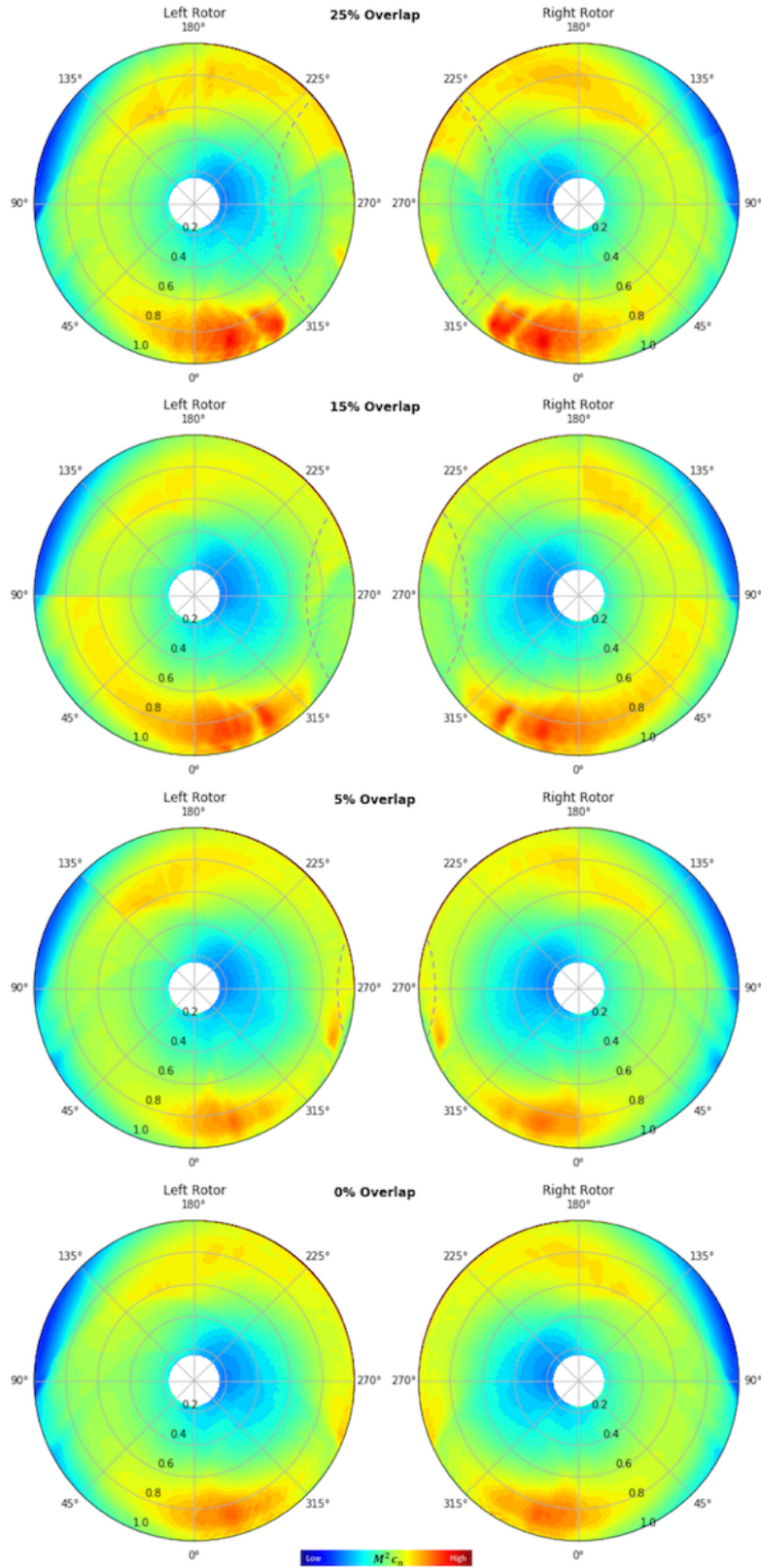


Figure 18: Rotor disk normal force coefficient for side-by-side rotors with different overlap distances. The grey dashed lines show the overlap zone.

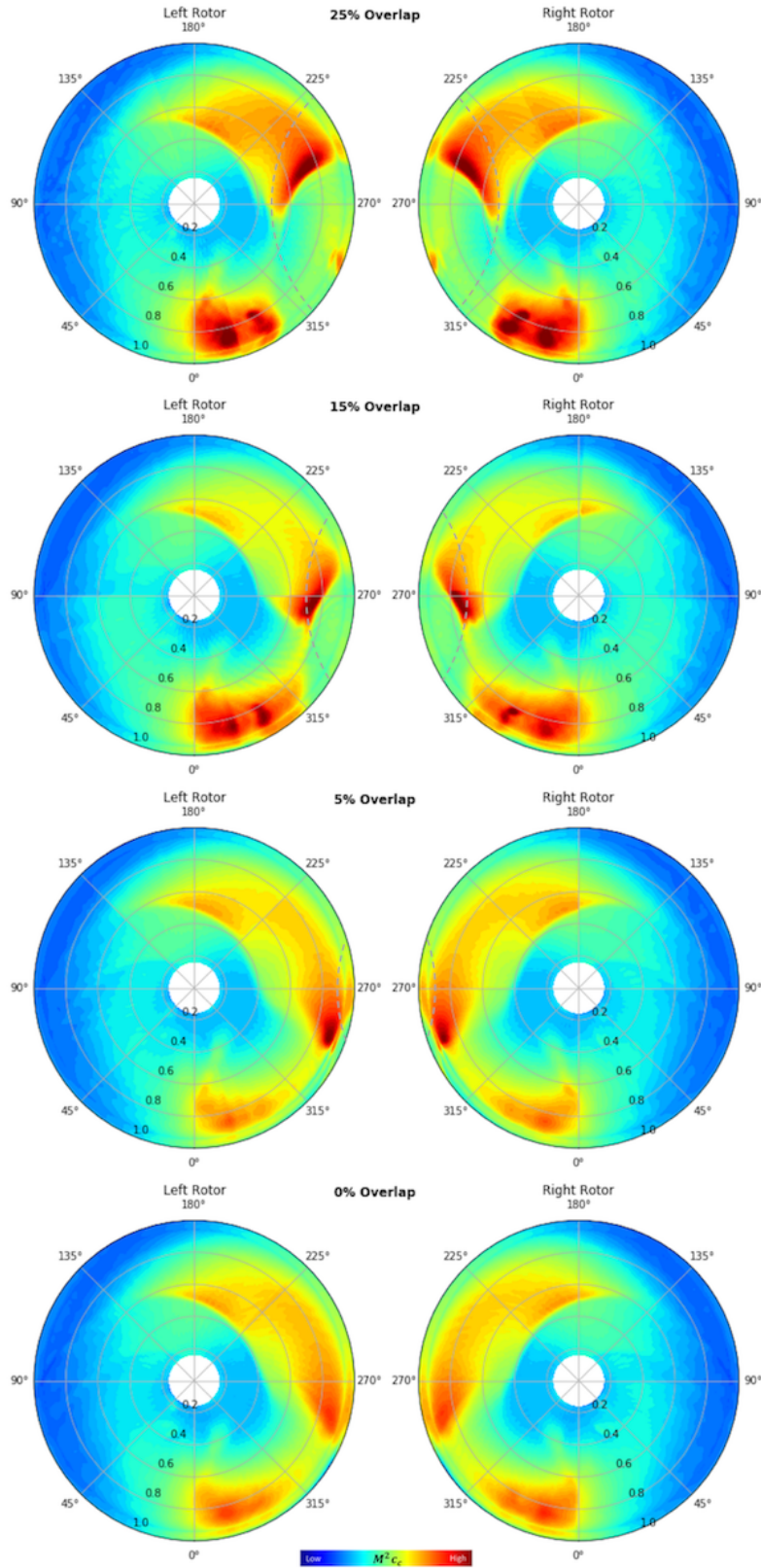


Figure 19: Rotor disk chord force coefficient for side-by-side rotors with different overlap distances. The grey dashed lines show the overlap zone.

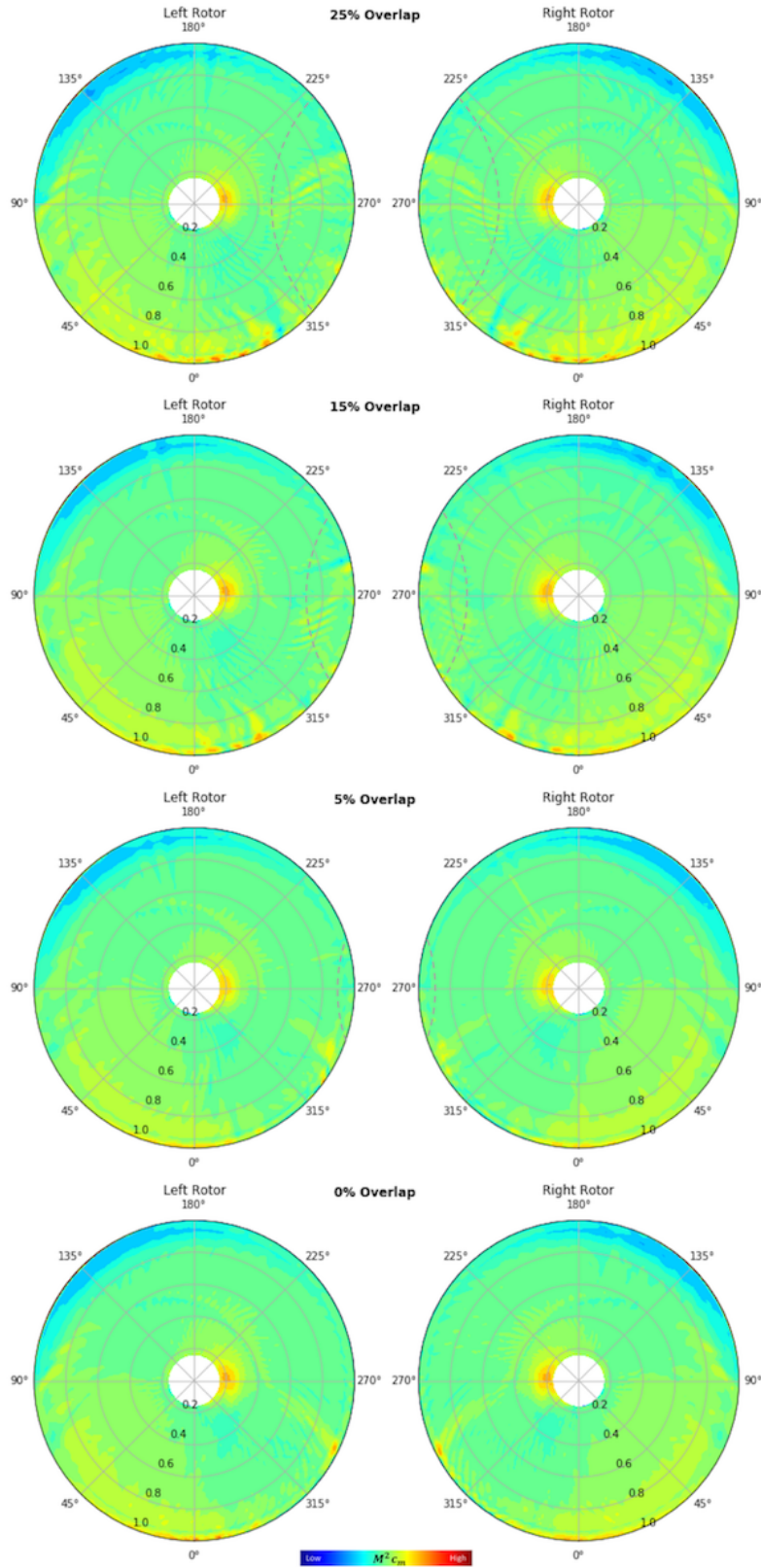


Figure 20: Rotor disk pitch moment coefficient for side-by-side rotors with different overlap distances. The grey dashed lines show the overlap zone.

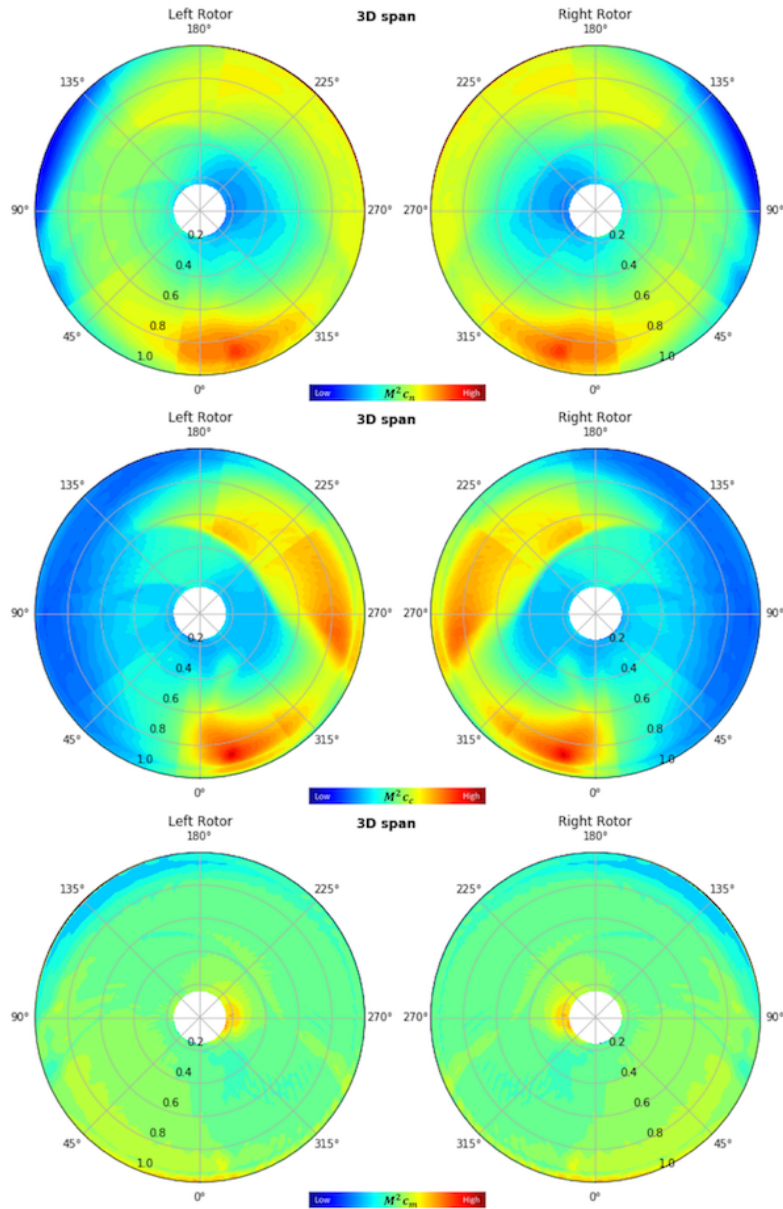


Figure 21: Rotor disk normal force coefficient (top), chord force coefficient (middle) and pitch moment coefficient (bottom) for side-by-side isolated rotors, with a wing span of $3D$.

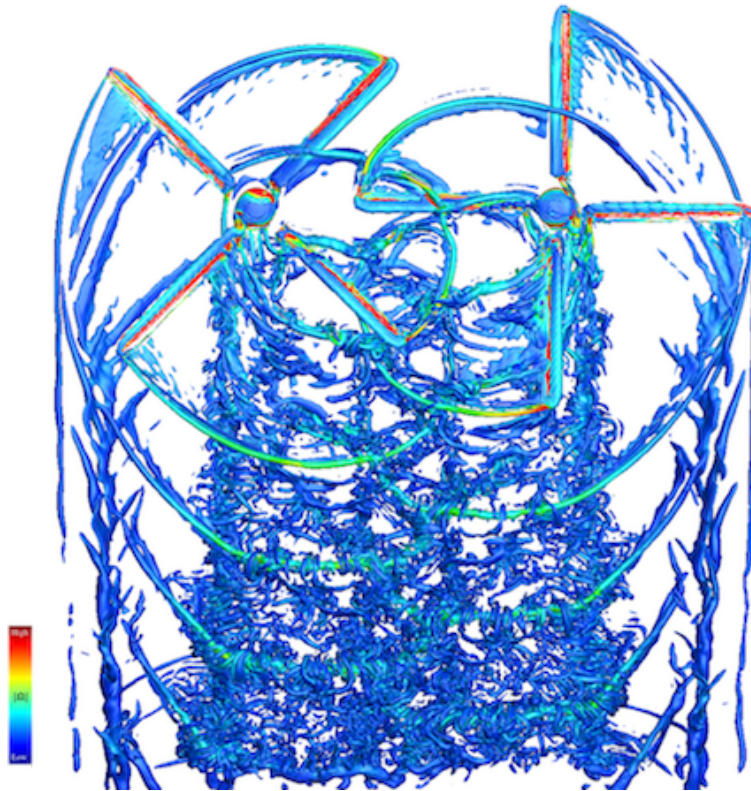


Figure 22: Vortex wake for two side-by-side rotors with 25% overlap.

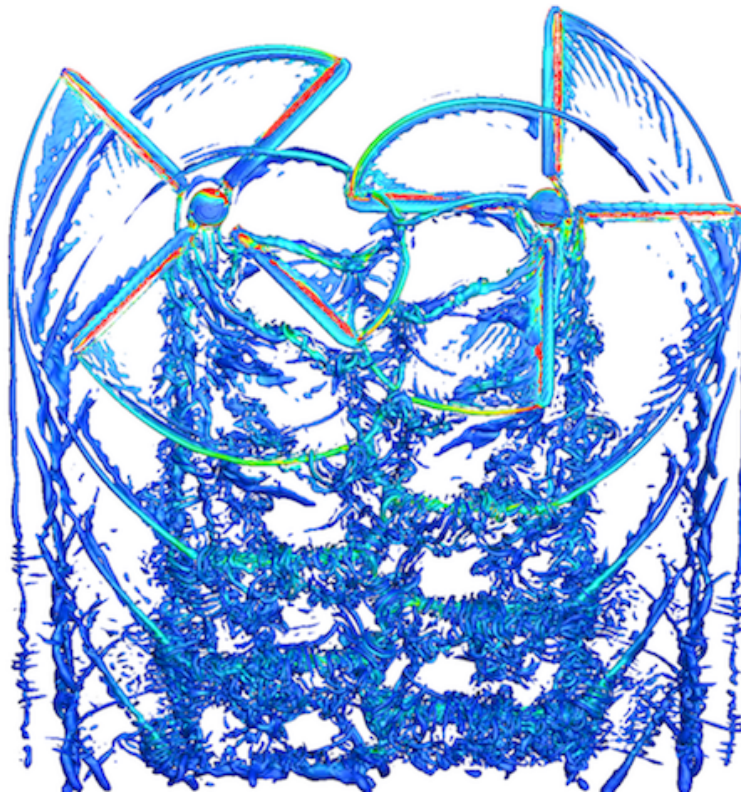


Figure 23: Vortex wake for two side-by-side rotors with 15% overlap.

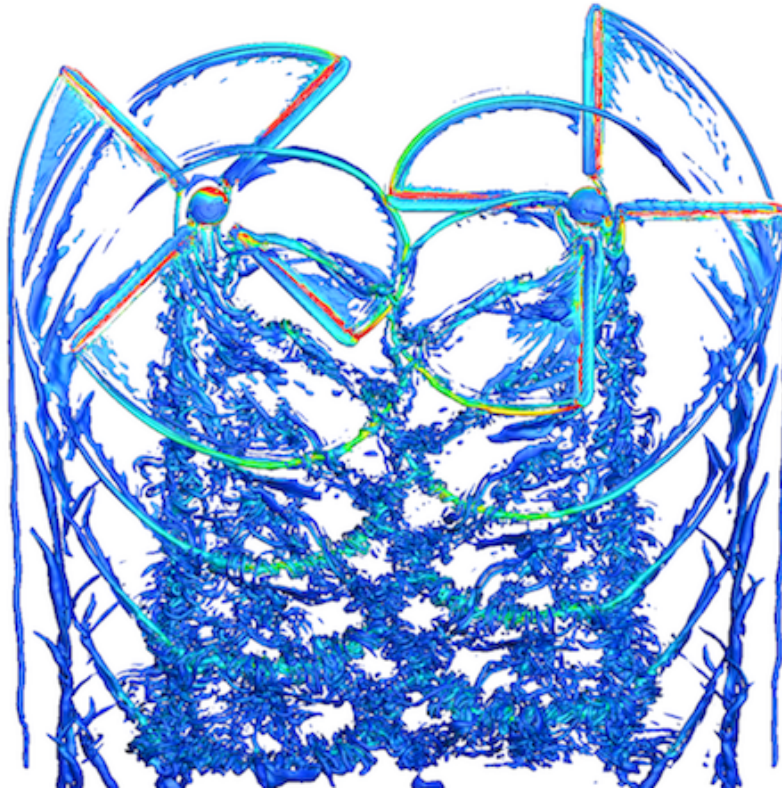


Figure 24: Vortex wake for two side-by-side rotors with 5% overlap.

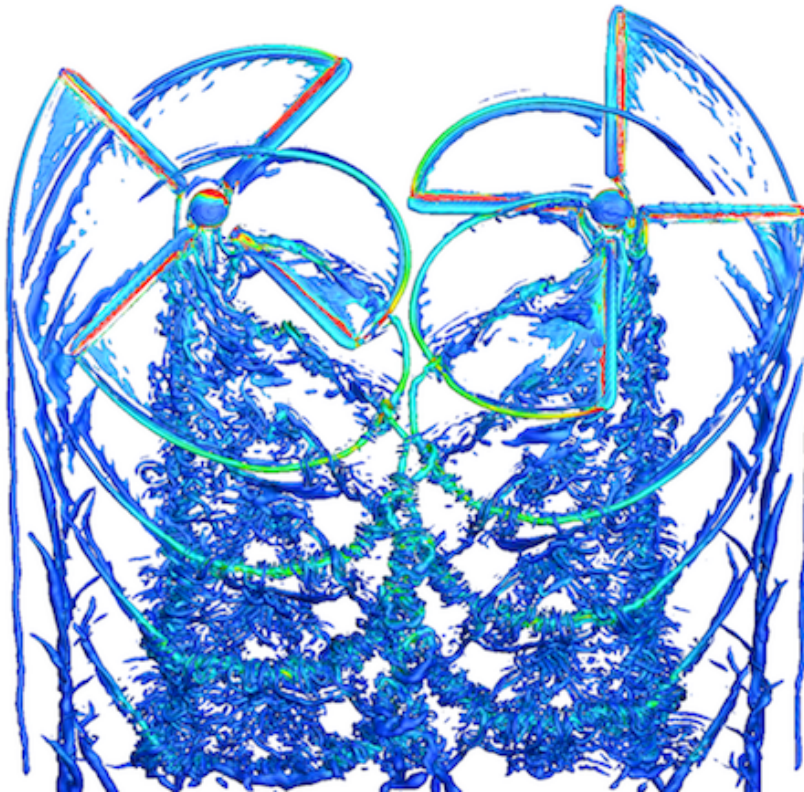


Figure 25: Vortex wake for two side-by-side rotors with 0% overlap.

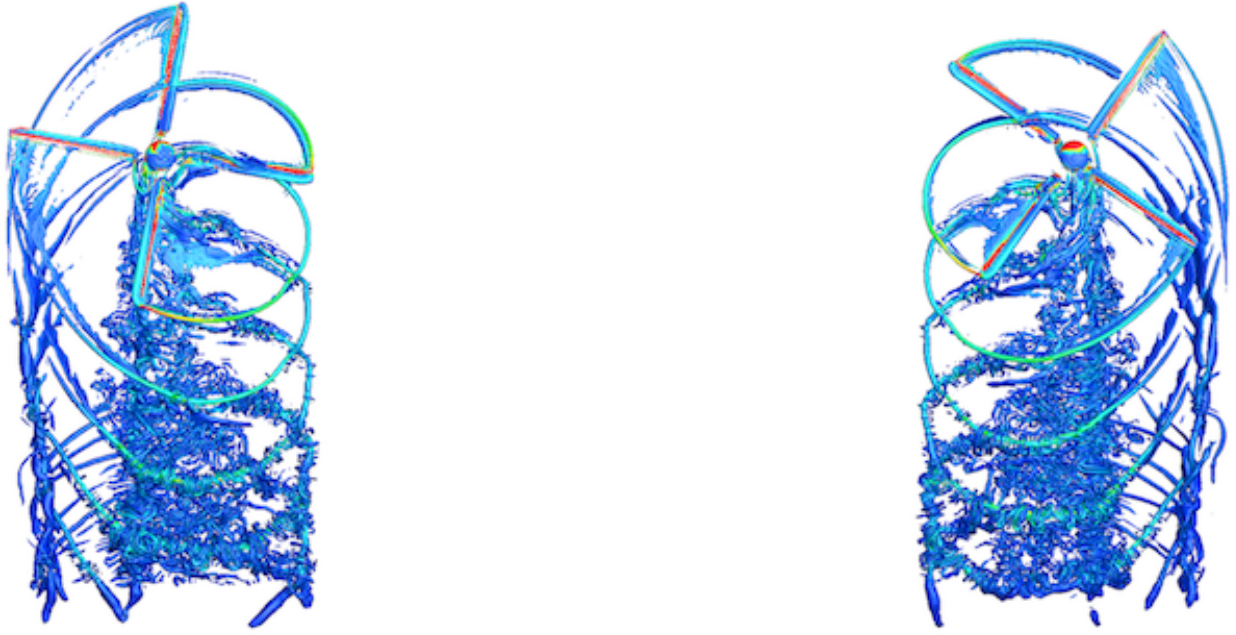


Figure 26: Vortex wake for two side-by-side isolated rotors.

The three BVI events can be easily found in Figure 22. Using the nomenclature from Figure 11, where blade 1 is the blade in the first quadrant ($0^\circ \leq \psi < 90^\circ$), blade 2 is the blade positioned in the second quadrant ($90^\circ \leq \psi < 180^\circ$), blade 3 is the blade positioned in the third quadrant ($180^\circ \leq \psi < 270^\circ$), and blade 4 is the blade positioned in the fourth quadrant ($270^\circ \leq \psi < 360^\circ$). The first BVI event happens near $\psi = 90^\circ$, see blade 2 ($\psi = 90^\circ$) from the right rotor: the blade encounters the vortex trailed by blade 3 from the same rotor. The second BVI event happens before $\psi = 270^\circ$; see blade 4 from the right rotor: this blade meets with the vortex shed by blade 4 from the left rotor (located at $\psi = 315^\circ$). As we decrease the overlap distance, the second BVI event is delayed in azimuth, see for example Figure 24 where the BVI event happens at $\psi = 270^\circ$. The third BVI event is harder to see, because it happens for an azimuth located between $270^\circ < \psi < 315^\circ$. It can still be discerned for blade 4 of the left rotor; see Figure 25 for the case with 0%, where the blade has already encountered the vortex from the previous blade (blade 1), from the same rotor. In the cases with some overlap, blade 4 will again encounter the vortex from blade 4 of the opposite rotor. The multiple BVI events will likely lead to increased noise. For the two side-by-side isolated rotors, Figure 26, only BVI from the same rotor occurs.

In conclusion, the wake in the overlap zone leads to unsteadiness in the flow, with significant blade-vortex interactions and therefore likely increased noise.

Performance

To finish the study of different overlap distances on side-by-side rotors for urban air mobility vehicles, the performance of the rotor systems are presented. The efficiency of the rotor system is measured using the rotor-to-lift drag ratio, defined as in equation 12.

L/D_e	25% overlap	15% overlap	5% overlap	0% overlap	Isolated
CAMRAD II free wake	9.43	10.05	9.76	9.60	8.94
Overflow-CAMRAD II	7.72	8.15	8.12	8.02	7.20

Table 3: Side-by-side performance calculations of the rotor system (right rotor + left rotor). The rotor efficiency in cruise, $L/D_e = WV/(P_i + P_0)$, is shown.

The calculated performance for each overlap are shown in Table 3. The trend obtained from the com-

prehensive analysis is confirmed here with the high-fidelity CFD results: the rotors with 15% overlap are the most efficient in cruise. That is, side-by-side rotors with 15% overlap are about 15% better than two side-by-side isolated rotors. Figure 27 shows the results from Table 3. Even if there is about 20% difference between the comprehensive code and the CFD results, the main motivation of this work was to confirm the performance improvement. It remains to validate these results with experiments.

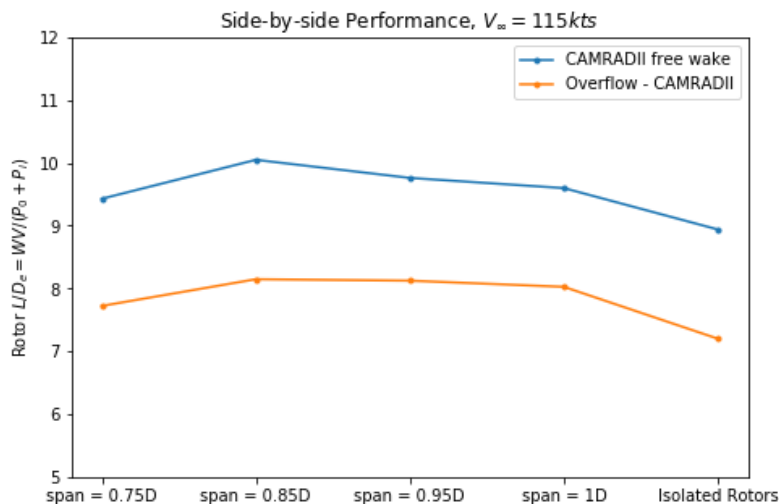


Figure 27: Side-by-side performance calculations of the rotor system (right rotor + left rotor). The rotor efficiency in cruise, $(L/D_e) = WV/(P_i + P_0)$, is shown.

C. Overflow - CAMRAD II Results: SbS Urban Air Taxi in Edgewise Flight

This final section presents NASA's urban air taxi concept with side-by-side rotors, for a span of $0.85D$. The complete vehicle is a complicated geometry as it has multiple components: the rotors, the fuselage, the engine, the tail, etc. The mesh generation process is very long and requires considerable expertise from the user in order to produce high quality meshes. In addition, the convergence of the flow solver is more difficult than the cases with only rotors.

The rotor disk normal force coefficient, chord force coefficient, and pitch moment coefficient are shown in Figure 28. It seems to follow a similar pattern as the side-by-side rotors without airframe. However, there are some differences. The overlapping regions seems to be more affected by the rotor-rotor interactions, see force coefficients near $\psi = 270^\circ$. This is probably due to the presence of components underneath the rotors like the engines, the wing, and the airframe. These components act as a ground effect on the rotors, increasing rotor efficiency and rotor-rotor interactions. The pitch moment coefficient does not seem to change much when adding the airframe.

The vortex wake for the full vehicle composed of overlapping rotors and airframe is shown in Figures 29a and 29b. Figure 29a shows the top view of the Q-criterion vorticity iso-surfaces colored by the vorticity magnitude. Some similarities in the wake geometry with the case of the side-by-side rotors without the airframe (Figure 23) can be observed, i.e., the BVI events seem to happen at comparable times. However, many more turbulent structures coming from the airframe are present: there is separated flow from the engines, junction vortices, and other complicated turbulent features.

Figure 29b shows an oblique view of the vortex wake colored by the pressure. The side-by-side urban air taxi offers some advantages compared to other UAM concepts: a more compact design with an increased efficiency in cruise might be one key factor enabling its feasibility. Although there are no validation data, the computational results may assist in future validation testing.

Finally, the comparison of the cruise performance of the side-by-side vehicle (rotors + airframe) with the side-by-side rotors, is shown in Table 4. The vehicle increases the rotor efficiency by 6%.

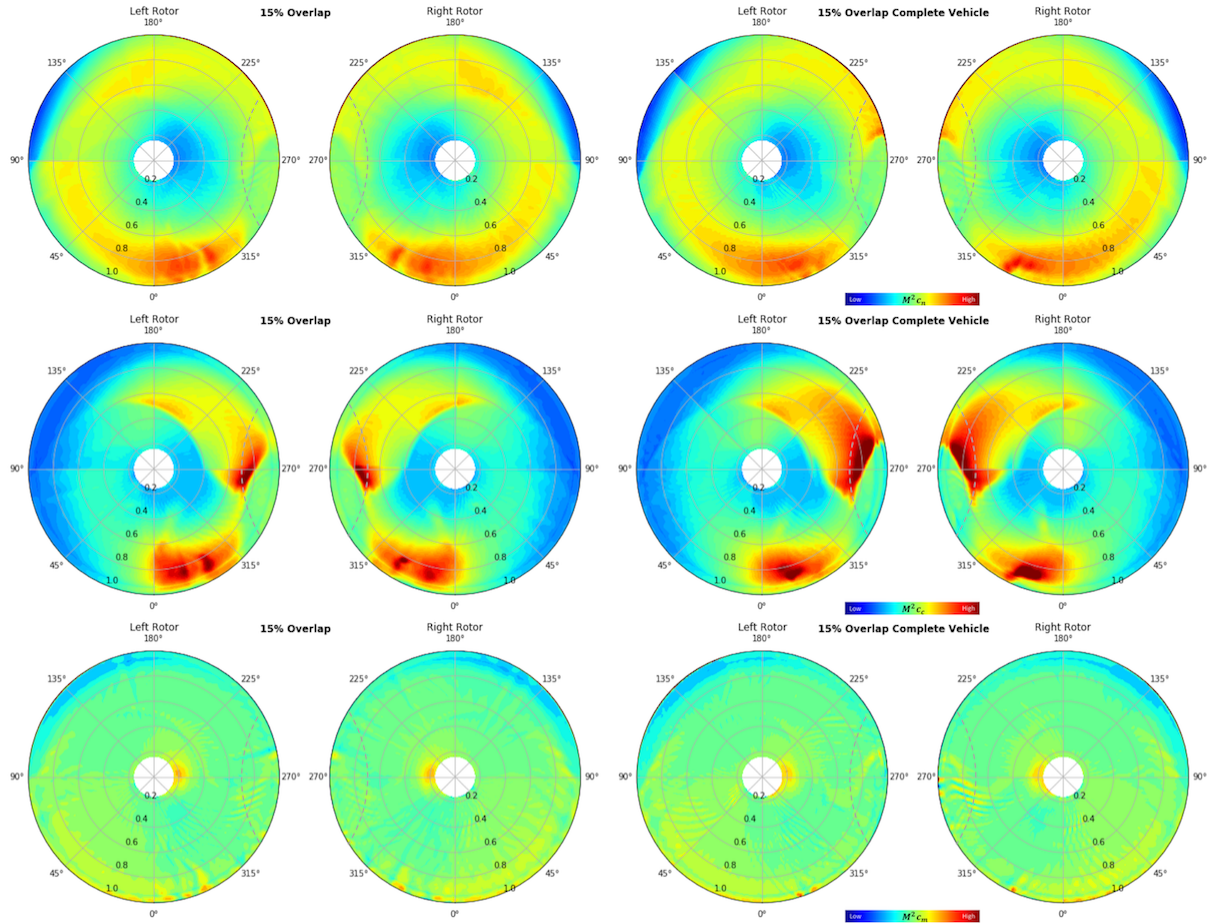
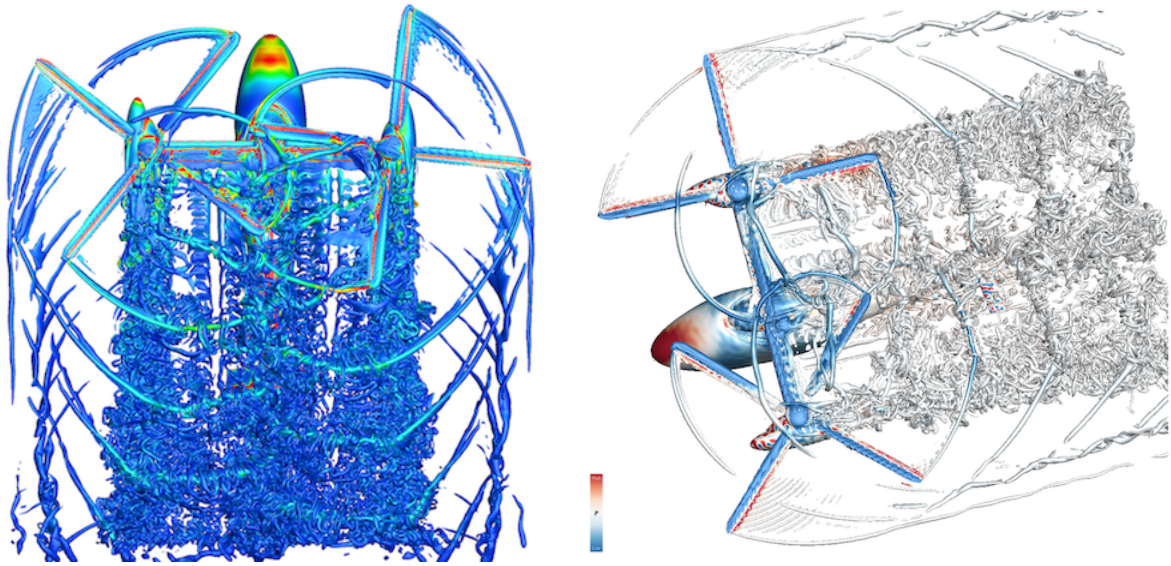


Figure 28: Rotor disk normal force coefficient (top), chord force coefficient (middle) and pitch moment coefficient (bottom) for the side-by-side urban air taxi with $0.85D$ span, or 15% overlap. The left column shows the force and moment coefficients for the side-by-side only rotors simulations with 15% overlap. The right column represents the forces and moments of the full vehicle with wing span of $0.85D$. The dashed grey lines show the overlap zone.



(a) Top view of the vortex wake. The Q-criterion vorticity iso-surfaces are colored with the vorticity magnitude. (b) Oblique view of the vortex wake. The Q-criterion vorticity iso-surfaces are colored with the pressure.

Figure 29: Vortex wake for the side-by-side urban air taxi with $0.85D$ span, or 15% overlap. The airframe adds complexity to the flow field observed.

L/D_e	15% overlap
CII free wake	10.05
Overflow - CII Only Rotors	8.15
Overflow - CII Complete Vehicle	8.67

Table 4: Cruise performance calculations of side-by-side rotors with 15% overlap. The rotor efficiency L/D_e is calculated from the simulations of CAMRAD II free wake, Overflow - CAMRAD II coupled for only the rotors, and Overflow - CAMRAD II for the complete vehicle.

VI. Summary

The effects of the rotor overlap distance of NASA's side-by-side urban air taxi concept have been analyzed. A loose coupled approach to simulate the flow of the twin rotor system in cruise conditions has been followed. The rotorcraft comprehensive code CAMRAD II and the overset finite-difference Navier-Stokes high-order accurate CFD solver Overflow have been coupled. CAMRAD II provides the blade motions and aircraft attitude to Overflow and Overflow accurately solves the flow, and the aerodynamic loads obtained with Overflow are sent as input to CAMRAD II, which recalculates the new trim solution and updates the blade motions and aircraft angles.

The airloads for different overlaps have been studied. The intermeshing region causes multiple blade-vortex interaction events, with vortices shed from the same and the opposite rotor. The opposite rotor BVI's event varies when the overlap distance is changed. The right and left rotors have similar airload distributions, and the small dissymmetries are probably caused by the turbulent character of the vortex wake.

The main features of the wake geometry with different overlap distances have been analyzed.

The performances of the rotors have been presented. First, the results with CAMRAD II have shown that overlapping rotors are more efficient in cruise than two isolated rotors, and the best configuration is for 15% rotor overlap. Then, for the best range cruise, the coupled CAMRAD II - Overflow simulations have confirmed this trend.

The computational results for the complete side-by-side vehicle have been introduced. Future work will include a more extensive analysis of the full vehicle, for different flight conditions.

The side-by-side urban air taxi is one of the concept vehicles expected to focus and guide NASA research activities in support of aircraft development for emerging aviation markets, in particular VTOL air taxi operations.

VII. Acknowledgements

This work was supported by the Revolutionary Vertical Lift Technology project. The computations utilized the Electra supercomputer at NASA Advanced Supercomputing Division. The authors would like to thank Brian Allan, Gloria Yamauchi, Chris Silva, and Eduardo Solis for helpful discussions.

References

- ¹Ventura Diaz, P., and Yoon, S., “High-Fidelity Computational Aerodynamics of Multi-Rotor Unmanned Aerial Vehicles”, AIAA Paper 2018-1266, The AIAA SciTech Forum 2018, Kissimmee, Florida, January 2018.
- ²Ventura Diaz, P., and Yoon, S., “A Physics-Based Approach to Urban Air Mobility”, The European Rotorcraft Forum, Paper 18, Delft, The Netherlands, September 2018.
- ³Yoon, S., Ventura Diaz, P., Boyd, D. D., Chan, W. M., and Theodore, C. R., “Computational Aerodynamic Modeling of Small Quadcopter Vehicles”, AHS Paper 73-2017-0015, The 73rd Annual AHS International Forum & Technology Display, Fort Worth, Texas, May 2017.
- ⁴Yoon, S., Chan, W. M., and Pulliam, T. H., “Computations of Torque-Balanced Coaxial Rotor Flow”, AIAA Paper 2017-0052, The 55th AIAA Aerospace Sciences Meeting, Grapevine, Texas, January 2017.
- ⁵Johnson, W., Silva, C., and Solis, E., “Concept Vehicles for VTOL Air Taxi Operations”, The AHS International Technical Meeting on Aeromechanics Design for the Transformative Flight, San Francisco, California, January 2018.
- ⁶Silva, C., Johnson, W., and Solis, E., “Multidisciplinary Conceptual Design for Reduced-Emission Rotorcraft”, The AHS International Technical Meeting on Aeromechanics Design for the Transformative Flight, San Francisco, California, January 2018.
- ⁷Johnson, W., *Helicopter Theory*, Dover Publications, 1994.
- ⁸Yoon, S., Chaderjian, N. M., Pulliam, T. H., and Holst, T. L., “Effect of Turbulence Modeling on Hovering Rotor Flows”, AIAA Paper 2015-2766, The 45th AIAA Fluid Dynamics Conference, Dallas, Texas, June 2015.
- ⁹Pulliam, T. H., “High Order Accurate Finite-Difference Methods: as seen in OVERFLOW”, AIAA Paper 2011-3851, June 2011.
- ¹⁰Chan, W. M., Gomez, R. J., Rogers, S. E., Buning, P. G., “Best Practices in Overset Grid Generation”, AIAA Paper 2002-3191, The 32nd AIAA Fluid Dynamics Conference, St. Louis, Missouri, June 2002.
- ¹¹Johnson, W., “Rotorcraft Aerodynamic Models for a Comprehensive Analysis”, American Helicopter Society 54th Annual Forum, Washington, D. C., May 1998.
- ¹²Potsdam, M., Yeo, H., and Johnson, W., “Rotor Airloads Prediction Using Loose Aerodynamics/Structural Coupling”, American Helicopter Society 60th Forum, Baltimore, Maryland, June 2004.
- ¹³Haines, R., and Dannenhoffer, J. F., “The Engineering Sketch Pad: A Solid-Modeling, Feature-Based, Web-Enabled System for Building Parametric Geometry”, AIAA Paper 2013-3073, The 21st AIAA Computational Fluid Dynamics Conference, San Diego, California, June 2013.
- ¹⁴Yoon, S. Lee, H. C., and Pulliam, T. H., “Computational Study of Flow Interactions in Coaxial Rotors”, The AHS Technical Meeting on Aeromechanics Design for Vertical Lift, San Francisco, California, January 2016.
- ¹⁵Yoon, S., Lee, H. C., and Pulliam, T. H., “Computational Analysis of Multi-Rotor Flows”, AIAA Paper 2016-0812, The 54th AIAA Aerospace Sciences Meeting, AIAA SciTech Forum, San Diego, California, January 2016.
- ¹⁶Spalart, P. R., Jou, W-H., Strelets, M., and Allmaras, S. R., “Comments on the Feasibility of LES for Wings and on a Hybrid RANS/LES Approach”, *Advances in DNS/LES*, Greyden Press, 1997, pp. 137-147.
- ¹⁷Spalart, P. R., “Strategies for Turbulence Modeling and Simulations”, *International Journal of Heat and Fluid Flow*, 21, 2000, pp. 252-263.
- ¹⁸Chaderjian, N., “Navier-Stokes Simulation of UH-60A Rotor/Wake Interaction Using Adaptive Mesh Refinement”, American Helicopter Society 73rd Annual Forum, Fort Worth, Texas, May 2017.